HOKKAIDO UNIVERSITY

Title	Gradient Coil Design Method Specifically for Permanent-Magnet-Type Low Field Portable MRI Brain Scanner
Author(s)	Kong, Xiaohan; Xu, Zheng; Shen, Sheng et al.
Citation	IEEE transactions on instrumentation and measurement, 72, 4000512 https://doi.org/10.1109/TIM.2022.3225042
Issue Date	2022-12-02
Doc URL	https://hdl.handle.net/2115/88598
Rights	© 2022 IEEE. Personal use of this material is permitted. Permission from IEEE must be obtained for all other uses, in any current or future media, including reprinting/republishing this material for advertising or promotional purposes, creating new collective works, for resale or redistribution to servers or lists, or reuse of any copyrighted component of this work in other works.
Type	journal article
File Information	Manuscript_final_TIM.pdf

Hokkaido University Collection of Scholarly and Academic Papers : HUSCAP

Gradient Coil Design Method Specifically for Permanent-magnet-type Low Field Portable MRI Brain Scanner

Xiaohan Kong(孔晓涵), Zheng Xu*(徐征), Sheng Shen(沈晟), Jiamin Wu(吴嘉敏),
Yucheng He(贺玉成), Liang Xuan(宣亮), and Hajime Igarashi*(五十嵐 一), *Member, IEEE*

Abstract*—ferromagnetic structures, particularly the anti-eddy plate, in a bi-planar permanent-magnet-type low-field (0.05 T) magnetic resonance imaging (MRI) brain scanner can distort the gradient field in the target region. This study aims to provide a new gradient coil design method that reduces ferromagnetic influences on gradient field linearity. Thus, a simplified model of electromagnetic (EM) structures of the permanent-magnet-type MRI scanners was established. By using precise analytical proof, the anti-eddy plate was reduced to a homogeneous magnetic plate. The overall effects of the EM structures, which can be represented by bi-planar magnetic plates, were evaluated. In sequence, the image magnetic dipole was first introduced to show the effects of anti-eddy plates were added to the conventional equivalent magnetic dipole (EMD) approach. A novel equivalent image magnetic dipole (EIMD) method was proposed to build the gradient coil pattern. The effect of ferromagnetic materials was predicted throughout the gradient coil design phase using the proposed method, and a high-linear gradient field was generated under real working conditions. The computational and experimental results showed that the gradient coil was linear when ferromagnetic structures were present. The effectiveness of the proposed method was demonstrated by comparing T1-weighted images of the conventional method to those of the proposed method. The proposed method reduced image distortion caused by nearby EM structures in bi-planar permanent-magnet-type low-field MRI systems and provided an effective and concise solution for gradient coil designs.

***Index Terms*—Magnetic resonance imaging; Brain Imaging; Inverse problems; Medical diagnosis; Optimization methods.**

I. INTRODUCTION

MAGNETIC resonance imaging (MRI) is an indispensable diagnostic tool because of its capacity to image physiological structures noninvasively and without radiation. Until recently, improved resolution and signal-to-noise ratio were achieved owing to powerful superconducting magnets, well-developed radio-frequency (RF), and gradient coil technologies [1], [2]. However, the strict operating environment requirements and weight limit flexibility and mobility. Moreover, the high maintenance costs prevent their use in low-income areas. Portable MRI devices can be used as supplements in high-field superconducting MRI. Compared to commonly used high-field MRI scanners (1.5 T and 3 T), low-field or ultra-low-field portable MRI is lightweight, movable, and provides low-cost MRI diagnostic services. There have been in-depth and effective investigations in this domain for these objectives [3]-[17]. For example, the active shielding technology has been realized, allowing low-field MRI devices to be used in unshielded electromagnetic (EM) environments [3]-[7], such as Intensive Care Units (ICUs), ambulances, and disaster sites. However, some problems remain to be studied, especially about the EM structure including gradient coil design. According to how the main magnetic field is generated, there are several varieties of low field or ultra-low field MRI equipment, such as electromagnet-type [8]-[10], Halbach-magnet-type [11]-[13], and bi-planar-magnet-type [3]-[5], [14]-[17]. The bi-planar magnet-type device is commonly used owing to its good magnetic field homogeneity, structural compactness, and imaging area openness.

The gradient coils in the MRI scanner generate linear gradient fields and provide spatial localization in the region of interest (ROI). Consequently, high linearity in the gradient field is required. In bi-planar magnet-type devices, switching gradient fields can cause considerable eddy currents in permanent magnets. For this reason, either active shielding coils or anti-eddy plates are commonly used to prevent the gradient field from entering the permanent magnets or other metal structures. Active shielding coils generate a reverse magnetic field to cancel the original field in the shielded areas. However, they may offset the field in the target region, resulting in a lower efficiency. Qualified shielding effects and efficiency can be obtained at similar time only when the distance between the main and shielding coil is considerable. Different from active shielding coils, the introduction of an anti-eddy plate is a

---

This study was supported by Japan Science and Technology Agency (JST) Support for Pioneering Research Initiated by the Next Generation (SPRING), Grant Number JPMJSP2119. It was also funded by the National Natural Science Foundation of China under grant number 52077023, the National Natural Science Foundation of Chongqing under grant number cstc2020jcyj-msxmX0340, and Shenzhen Science and Technology Innovation Commission under grant number CJGJZD20200617102402006.

Xiaohan Kong is with Graduate School of Information Science and Technology, Hokkaido University, Sapporo 060-0814, Japan. Sheng Shen is with Massachusetts General Hospital, MA 02129, USA. Jiamin Wu and Yucheng He are with Shenzhen Academy of Aerospace Technology, Shenzhen 100048, China. Liang Xuan is with School of Electrical Engineering, Chongqing University, Chongqing 400044, China, *Zheng Xu is with School of Electrical Engineering, Chongqing University, Chongqing 400044, China. (Correspondence e-mail: xuzheng@cqu.edu.cn). *Hajime Igarashi is with Graduate School of Information Science and Technology, Hokkaido University, Sapporo 060-0814, Japan. (Correspondence e-mail: igarashi@ssi.ist.hokudai.ac.jp).

more direct and convenient method for gradient field shielding, whereas the high-permeability material of the anti-eddy plate may distort the gradient field in the target region. The gradient coils designed by the conventional method lose their good linearity when they are installed on the anti-eddy plate and eventually lead to image distortion, particularly for X and Y gradient coils. Hence, the magnetic effect of the anti-eddy plate should be considered during the gradient coil design process. Although there are no anti-eddy plates in devices that use active shielding coils to shield gradient fields, the ferromagnetic effects of the pole piece and iron yoke should be considered during the design process.

The gradient design methods can be divided into two categories depending on whether the coil is discrete [18] or distributed [19]-[23]. The distributed winding method is more flexible because the coil shapes do not need to be pre-determined. The distribution method includes the stream function [19], target field [20], [21], and equivalent magnetic dipole (EMD) methods (also known as equivalent magnetization current, EMC) [22-24]. The EMD method was introduced by Stuart Crozier and Hector Sanchez Lopez to design gradient coils for MRI devices [22]. However, when the aforementioned methods were applied to gradient coil designs, the effect of magnetic materials was seldom considered. Neglecting this effect would result in unqualified gradient field linearity and image distortion.

There have been studies of the influence of ferromagnetic materials in their coil designs. Zhao [25] and Yang [26] described the design of the active shielding coils to produce a practically zero-field environment. In these studies, they utilized the image method [27], [28] to consider the ferromagnetic effects of a magnetic shielding room and a closed magnetically shielded cylinder, respectively. However, the image representation for the laminated structures such as anti-eddy plates has not been considered. Additionally, the gradient coil design in the low-field MRI system considering ferromagnetic effects has not been performed.

In this study, a complete procedure for designing gradient coils specifically for low-field MRI devices was presented, wherein the effect of ferromagnetic materials, particularly anti-eddy plates, was considered. The original contributions are as follows:

(a) The laminated anti-eddy plate was simplified to a homogenized magnetic plate, where the equivalent permeability was extracted by analytical solution. This reduced the structure complexity obviously;

(b) The image current loops were adopted to represent the ferromagnetic effects of the homogenized magnetic plate, based on the image current method;

(c) The equivalent image magnetic dipole (EIMD) method was proposed based on the two points mentioned above. This method considered the ferromagnetic effects by adding the image magnetic dipoles (image current loops) as magnetic field source;

(d) The proposed EIMD method was applied to a real low-field MRI device. The field measurement and imaging results showed that this method works well to reduce the field distortion caused by the ferromagnetic materials.

II. PERMANENT-MAGNET-TYPE MRI DEVICE

In Fig. 1 (a), the EM structure of the bi-planar magnet-type low-field MRI device is presented. The main EM structures include permanent magnets, gradient coils, and RF coils. A side view of the detailed structure and corresponding sizes are shown in Fig. 1 (b). The functions of each part of the device are as follows. (i) The bi-planar permanent magnets generate a vertically homogeneous magnetic field in the ROI. (ii) The gradient coils produce linear gradient fields in three vertical directions (x, y, and z) in the ROI. The spatial variation in the magnetic field allows the localization of image slices, phase encoding, and frequency encoding. (iii) The RF coils (excitation and receive coils) generate alternating fields for magnetic resonance and receive RF signals from the samples; (iv) Anti-eddy plates made of laminated vertical silicon steel sheets shield the gradient field and reduce eddy currents. (v) The stainless-steel iron yoke guides the static magnetic flux to form a closed loop. (vi) The pole piece, composed of non-alloy quality steel, improves the uniformity of the magnetic field. (vii) The shimming ring made from a material similar to that of the pole piece concentrates the magnetic flux at the target region. Owing to the high permeability of the anti-eddy plates, pole piece, shimming ring, and iron yoke, their influence on the gradient field is evident. However, the entire structure is too complex to be represented analytically. A simplified model was presented to represent these effects.

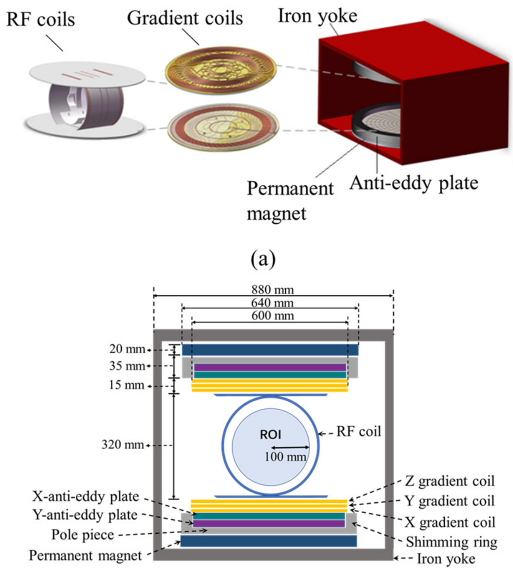

(a)

(b)

Fig. 1. Main structure of a low-field MRI system in (a) three-dimensional view, (b) side view.

The anti-eddy plate is the closest ferromagnetic structure to the gradient coils, as shown in Fig. 1 (b), with a higher permeability than that of other materials. This considerably affects the gradient field and image. The homogenized permeability of the anti-eddy plate needed for the proposed design method was evaluated.

A. Anti-eddy plates modeling

An anti-eddy plate, also called the shielding plate, is used to shield the permanent magnets and pole pieces from the gradient field to reduce the eddy current effect. It is made of multiple thin, high permeability silicon-steel sheets that are laminated together but insulate each other.

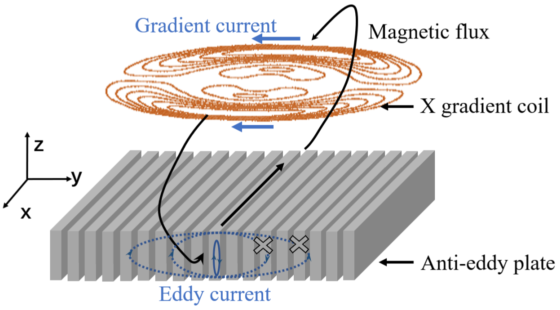

Fig. 2. Structures of X gradient coil and corresponding X anti-eddy plate (in the X anti-eddy plate, the magnetic flux goes along the x-direction due to its high permeability).

Fig. 2 shows the structures of the X gradient coil and X anti-eddy plate, wherein the magnetic field is constrained in the anti-eddy plate owing to its high permeability in the *x*-direction. Moreover, the eddy current induced in the plate is cut off by the air gap (dotted blue circle) and is limited to the thin area of the steel sheets (blue circle). This special structure maintains high permeability but reduces electrical conductivity. The Y and X gradient coils generally have a similar structure. As for the Z gradient coil, the shielding effect is the superposition of that of the X and Y anti-eddy plates put together. Hence, the analyses that follow will only focus on the X gradient coil. Evaluating the laminated structure using the finite element method (FEM) is difficult; therefore, we employed a homogenized model by extracting the homogenized permeability using an analytical solution, as shown in Fig. 3. Their thicknesses are the same and defined as *w*. The homogenized permeability along the laminated direction $\mu_{\parallel}$ is greater than that in the perpendicular direction $\mu_{\perp}$. Consequently, they must be evaluated separately. t_{steel} and t_{gap} represent the thicknesses of the steel sheets and air gap, and μ and μ_0 denote the permeability of the steel sheets and vacuum, respectively.

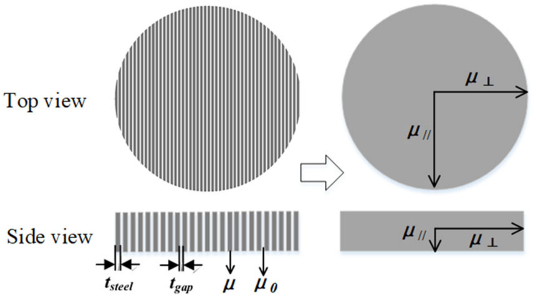

(a) (b)

Fig. 3. Top and side views of (a) the laminated steel sheets and (b) homogenized plates.

The homogenized permeability along the lamination and vertical directions $\mu_{\parallel}$ and $\mu_{\perp}$, respectively, can be obtained using (1) and (2). Detailed formulas are provided in the Appendix.

$$\mu_{\parallel} = \alpha\mu + (1-\alpha)\mu_0 \tag{1}$$

$$\mu_{\perp} = \frac{\mu\mu_0}{\alpha\mu_0 + (1-\alpha)\mu} \tag{2}$$

where α is the filling rate (volume fraction) of the laminated structure, calculated as:

$$\alpha = \frac{t_{steel}}{t_{steel} + t_{gap}} \tag{3}$$

$\mu_{\parallel r}$ and $\mu_{\perp r}$ are defined as the relative homogenized permeability along the lamination and vertical directions.

$$\mu_{\parallel r} = \frac{\mu_{\parallel}}{\mu_0} \tag{4}$$

$$\mu_{\perp r} = \frac{\mu_{\perp}}{\mu_0} \tag{5}$$

In order to verify the accuracy of the homogenization method, four different anti-eddy plates were considered to compare the analytical results with the finite element calculations. The steel sheet used in this permanent-magnet-type MRI device is 27RK095 electrical steel produced by BAO STEEL, CHINA. It has a relative permeability μ_r of 40000 and a thickness t_{steel} of 0.27 mm. We set t_{steel} and μ_r as constants, then $\mu_{\parallel r}$ and $\mu_{\perp r}$ are determined by t_{gap}. Four cases have different t_{gap}, causing their homogenized permeability to vary. The parameters of these four cases are listed in Table I. In the lamination direction, the increase in t_{gap} leads to a decline in $\mu_{\parallel r}$. In the perpendicular direction, the $\mu_{\perp r}$ remained low, which is close to the vacuum.

TABLE I
PARAMETERS OF FOUR CASES

Case Number	t_{steel} (mm)	t_{gap} (mm)	α	$\mu_{//r}$	$\mu_{\perp r}$
1	0.27	2.43	0.1	4000	1.11
2	0.27	10.54	0.025	1000	1.02
3	0.27	21.37	0.0125	500	1.01
4	0.27	43.13	0.0062	250	1.01

Taking the X gradient coil as an example, the magnetic flux along the laminated direction (*x*-direction) is the absolute dominant component in the region of steel sheets. Hence, steel sheets were simplified by a homogenized plate that had isotropic permeability $\mu_{\parallel r}$, the permeability along the perpendicular direction $\mu_{\perp r}$ was neglected. The laminated and homogenized models shown in Fig. 4 were analyzed using the FEM to verify the homogenization. In the homogenized model, the laminated structure was replaced with a homogenized plate with an anisotropic permeability $\mu_{\parallel r}$.

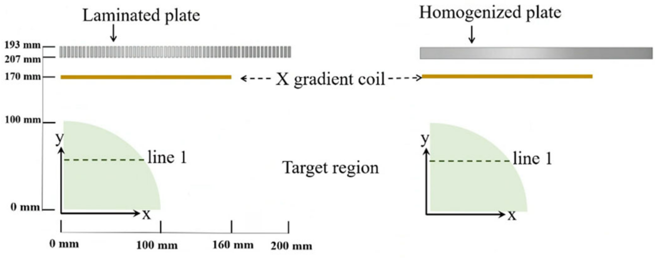

(a) (b)

Fig. 4. Models used to verify the homogenized permeability. (a) Laminated and (b) homogenized models

In our system, the static magnetic field is along the z-direction. For the X gradient coil, the z-component of gradient magnetic field induction (B_z) varies linearly along the x-direction. Superposing B_z to the static field causes a frequency variation of protons, a slice can be selected perpendicular to the gradient direction. Thus, we here pay attention to B_z.

For the four cases with different permeability, the magnetic field B_z along line 1 was plotted in Fig.5 to compare the B_z of homogenized and laminated models. The solid lines represent B_z in the homogenized models, while the dotted lines represent those of the laminated models. All the cases have good agreements with a maximum error lower than 1%. The curves in the blue dotted box are enlarged to see the discrepancies (located in the right lower side), which decrease from case 1 to case 4, wherein the t_{gap} gradually increases. This indicates that this homogenized model has higher accuracy when the steel sheets are more closely laminated.

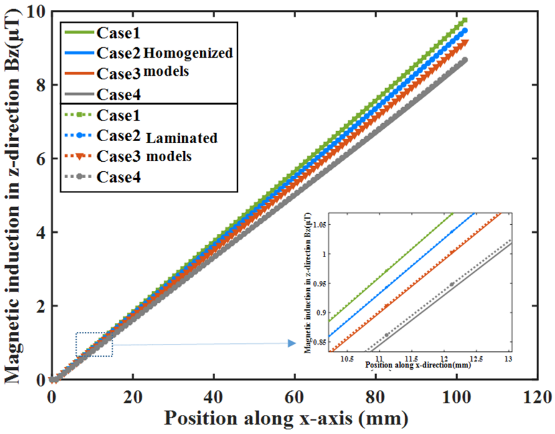

Fig. 5. Simulated B_z comparison between laminated and homogenized models along line 1.

In the permanent-magnet-type MRI device, the permeability of the silicon-steel sheets is 0.05 H/m and the relative permeability μ_r is 40000. The thicknesses of steel sheets t_{steel} and air gap t_{gap} are 0.27 mm and 0.02 mm, respectively. Hence, the filling rate α was calculated to be 0.931.

According to (4) and (5), the homogenized relative permeability in the lamination direction $\mu_{\parallel r}$ was 37200, whereas the relative permeability $\mu_{\perp r}$ is 14.5 in the perpendicular direction. For the X gradient coil, the magnetic flux mainly goes along the lamination direction, and the anti-eddy plate can be replaced by a homogenized metal plate with an isotropic permeability of 37200.

To verify the calculation results, the measurement platform shown in Fig. 6 was established. A Gauss meter probe (FW.Bell8030, resolution: 0.1nT, accuracy: ± 0.05% of reading) was fixed on a three-dimensional (3D) step motor and the current in the X gradient coil was 1 A. B_z was measured on the observation surface and compared to simulation results. As illustrated in Fig. 7, the simulation model replaced the X anti-eddy plate with a homogenized plate and had an isotropic relative permeability of 37200.

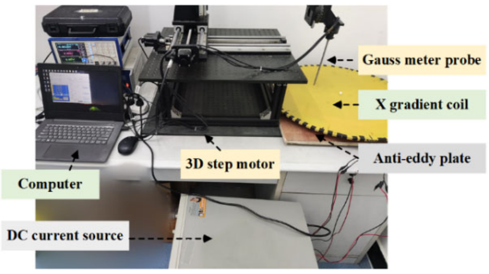

Fig. 6. Magnetic field measurement platform.

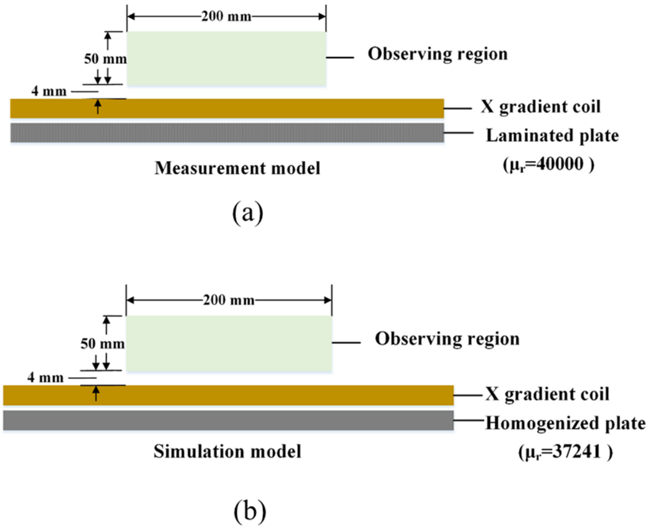

(a)

(b)

Fig. 7. Model comparison between (a) measurement and (b) simulation models.

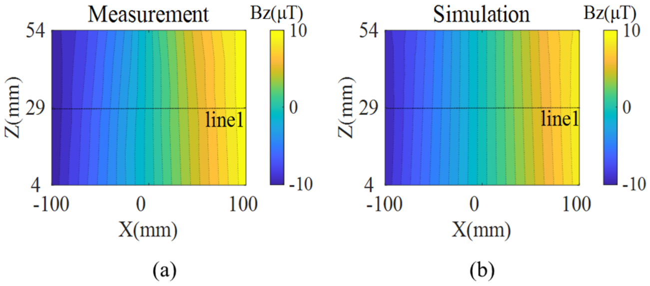

(a) (b)

Fig. 8. Magnetic field comparison between (a) measurement and (b) simulation results.

As shown in Fig. 8, B_z in the observed surface was compared and the measured magnetic field had a similar distribution to that of the simulation. The normalized B_z of measurement and simulation, along with the absolute errors, are shown in Fig. 9. Overall, the measured and simulated magnetic fields have a good agreement. The absolute errors show a random distribution along the x-axis and are mainly caused by the errors in the real measurements. The majority of measurement points have an error less than 4%. This proved that the homogenized model is a good imitation for the original laminated model.

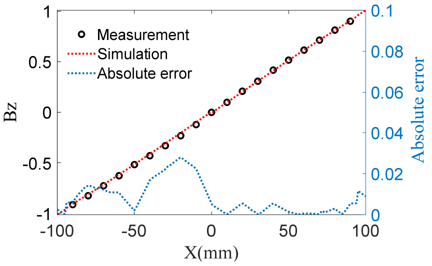

Fig. 9. Magnetic field comparison between measurement and simulation along line 1 (normalized by the maximum B_z).

B. Model simplification

In Part A, a homogenized model of the anti-eddy plate was established. Subsequently, the entire structure was evaluated. The permeability values were listed in Table II.

TABLE II
PERMEABILITY OF EM STRUCTURES

	Structure name	*Material type*	*Relative permeability*
1	Anti-eddy plate	Silicon steel sheets	37200
2	Shimming ring	Non-alloy quality steel	2000
3	Pole piece	Non-alloy quality steel	2000
4	Iron yoke	Stainless steel	1000
5	Permanent magnet	SmCo magnets	≈ 1

The relative permeability of the anti-eddy plate is higher than that of the other structures. Consequently, almost all the magnetic flux is confined in it. The complete magnetic structure can be simplified to a pair of homogenized plates, whose relative permeability equals that of anti-eddy plates $\mu_{\parallel r}$, and whose thickness and positions are same with those of the anti-eddy plates. Subsequently, the effects of the homogenized plates can be represented as image currents, based on the image current method [27], [28], as depicted in Fig. 10.

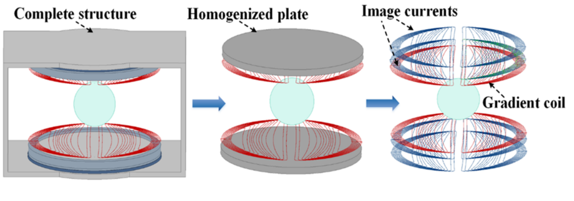

(a) (b) (c)

Fig. 10. Simplification process: (a) complete, (b) simplified (parallel magnetic plates), and (c) image current models.

The first layer of the image current is located at a distance of $2z_0$ from the coil and carries a current of αI, where $\alpha = (\mu_{\parallel r} - 1)/(\mu_{\parallel r} + 1)$. The remaining image currents are located $2w$ apart and carry a current of $-\alpha^{i-3}(1-\alpha^2)I$. They are added to compensate for the error due to the finite thickness of the magnetic plate, where i is the number of layers, w is the thickness of the magnetic plate, and z_0 is the distance between the gradient coil and homogenized plate.

In conclusion, a simplified model for gradient coil design was defined, wherein the effects of the anti-eddy plates were represented as a pair of homogenized magnetic plates. These can be further presented as image currents. Based on this, a new gradient coil design method is described in chapter III.

III. EQUIVALENT IMAGE MAGNETIC DIPOLE METHOD

The proposed method is based on the conventional EMD method [4], [5], which is summarized as follows: (i) the coil region is subdivided into Q small current loops (considered as magnetic dipoles); (ii) the loop currents, with width a and thickness h are determined such that the generated field matches the target field, and (iii) the coil path is obtained from the optimal current distribution. This procedure is schematically illustrated in Fig. 11.

The two-dimensional current field on the surface of the gradient coil region is represented by $\boldsymbol{J}_s$, which satisfies the following equation [23]:

$$\nabla \cdot \boldsymbol{J}_s = 0. \quad (6)$$

The stream function S [19] is defined to express $\boldsymbol{J}_s$ as follows:

$$\boldsymbol{J}_s = \nabla \times (S\boldsymbol{n}) \, , \quad (7)$$

where $\boldsymbol{n}$ is a unit normal vector. The contour plot of S results in a winding pattern. The current density $\boldsymbol{J}_s$ is expressed by magnetization $\boldsymbol{M}$ of the magnetic dipole, as follows [23]:

$$\boldsymbol{J}_s = h\nabla \times \boldsymbol{M}. \quad (8)$$

where h represents the thickness of a single layer of the magnetic dipole. The relationship between S and $\boldsymbol{M}$ [22] is:

$$\boldsymbol{M} = \frac{S\boldsymbol{n}}{h} \, . \quad (9)$$

Moreover, $\boldsymbol{M}$ can be represented by the dipole moment as:

$$\boldsymbol{m} = \boldsymbol{M}a^2h = a^2S\boldsymbol{n} \, . \quad (10)$$

The magnetic flux density produced by the magnetic dipole is expressed by the following equation:

$$\boldsymbol{B}(\boldsymbol{r}) = -\frac{\mu_0}{4\pi} a^2 S(\boldsymbol{r}_q) \nabla \frac{\boldsymbol{n}_q \cdot (\boldsymbol{r} - \boldsymbol{r}_q)}{|\boldsymbol{r} - \boldsymbol{r}_q|^3} , \qquad (11)$$

where $\boldsymbol{r}$ is the position vector at the target point and the quantities relevant to the magnetic dipoles are indexed by q. The magnetic flux density in the target region is a superposition of the fields produced by all magnetic dipoles [22], that is:

$$\boldsymbol{B}(\boldsymbol{r}) = \frac{\mu_0 a^2}{4\pi} \sum_{q=1}^{Q} \boldsymbol{c}(\boldsymbol{r}, \boldsymbol{r}_q) S(\boldsymbol{r}_q) , \qquad (12)$$

where

$$\boldsymbol{c}(\boldsymbol{r}, \boldsymbol{r}_q) = -\nabla \frac{\boldsymbol{n}_q \cdot (\boldsymbol{r} - \boldsymbol{r}_q)}{|\boldsymbol{r} - \boldsymbol{r}_q|^3} . \qquad (13)$$

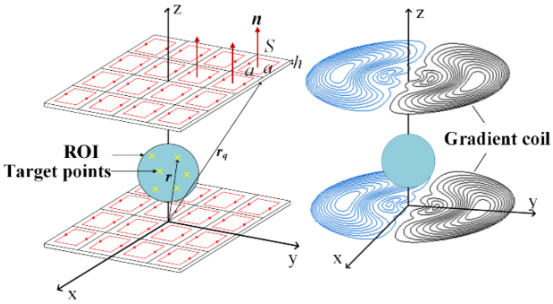

Fig. 11. Schematic representation of EMD method.

As the loop currents in the gradient coil region are the only sources of the magnetic fields expressed in (11) and (12), the conventional EMD method does not consider the influence of the magnetic material. To include this influence in the optimization model, the EIMD method was introduced.

According to the well-known image current method, the influence of the magnetic plate beneath the magnetic dipole can be represented as image current loops, as depicted in Fig.12, where we define the image current loops as equivalent image magnetic dipoles. To model the magnetic material, we place the first image magnetic dipole (represented using green solid lines) with equivalent current αI, where $\alpha = (\mu_{\parallel r} - 1)/(\mu_{\parallel r} + 1)$. To consider the finite thickness w of the magnetic plate, we place the image magnetic dipoles (represented using the green dotted line) with equivalent current, $-\alpha^{2i-3}(1-\alpha^2)I$ located $2w$ apart [27], [28]. When $\mu_{\parallel r}$ is sufficiently large, only the first image current must be considered. The magnetic moment located at the i-th layer is indicated by $\boldsymbol{m}_i$, where $\boldsymbol{m}_1$ has the same direction as that of $\boldsymbol{m}$, and others have the inverse direction.

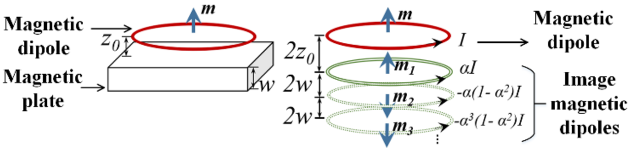

Fig. 12. EIMD method.

Considering the image currents in the gradient coil design, the stream function S_i is introduced, corresponding to the i-th image current and defined by the following equation:

$$S_i = \begin{cases} \alpha S, i = 1 \\ -\alpha^{2i-3}(1-\alpha^2)S,\ i = 2, 3, \dots \end{cases} \qquad (14)$$

Compared to the conventional EMD method depicted in Fig. 11, the effects of the magnetic plates are represented as image magnetic dipoles, in addition to the gradient coil, as depicted in Fig. 13.

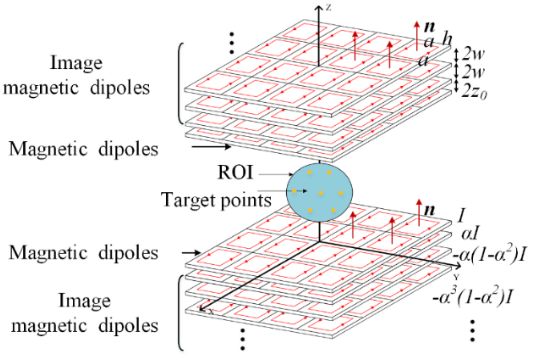

Fig. 13. Schematic representation of the EIMD method.

The magnetic field in the target region is computed from the superposition of the fields produced by the current loops. At the target point $\boldsymbol{r}$, the magnetic flux density is expressed as:

$$\boldsymbol{B}(\boldsymbol{r}) = \frac{\mu_0 a^2}{4\pi} \left(\sum_{q=1}^{Q} \boldsymbol{c}(\boldsymbol{r}, \boldsymbol{r}_q) S_q(\boldsymbol{r}_q) + \sum_{i=1}^{L} \sum_{t=1}^{T} \boldsymbol{c}(\boldsymbol{r}, \boldsymbol{r}_{ti}) S_i(\boldsymbol{r}_{ti}) \right), \qquad (15)$$

where T and L denote the number of image magnetic dipoles for a single layer and the number of layers, respectively, and $\boldsymbol{r}_{ti}$ denotes the position vector of the t-th small loop on the i-th layer. The second term in (15) represents the influence of the magnetic plate.

The optimization problem is defined as:

$$F = \sum_{n=1}^{N} |\boldsymbol{B}_n - \boldsymbol{B}_{target}|^2 + \lambda W_M \to \text{min.}, \qquad (16a)$$

$$W_M = \frac{1}{2} \int \boldsymbol{A} \cdot \boldsymbol{J}_s \, dV, \qquad (16b)$$

$\boldsymbol{B}_{target}$ is the ideal X gradient field in the n-th target point, which can be expressed by

$$\boldsymbol{B}_{target} = x_n \boldsymbol{G}_x \qquad (17)$$

where $\boldsymbol{G}_x$ is the required field gradient per meter in the x-direction, and x_n is the x-coordinate of n-th target point. W_M is the magnetic field energy of the current loops, λ is the regularization coefficient, and $\boldsymbol{A}$ is the vector magnetic potential relevant to the magnetic dipoles. When λ decreases, the magnetic field approaches the target field $\boldsymbol{B}_{target}$, whereas when it increases, the magnetic field energy decreases, thereby increasing the gradient switching speed. In (16), stream function S is the unknown function to be optimized. As presented in (7), the coil pattern can be obtained by drawing the contour line of *S*.

IV. GRADIENT COIL DESIGN

The X-gradient coil design process was considered as an example. The X-gradient coil generating the gradient field B_z with a linear spatial variation in the *x*-direction, was designed based on the proposed method. During the imaging process, the maximum gradient amplitude exists in the slice-selection gradient. Based on the formulas from [29], the slice-selection gradient amplitude G_{slice} is determined by the RF pulse bandwidth Δf and the minimum excitation slice thickness Δz. Additionally, Δf is determined by the bandwidth product $T\Delta f$ and pulse width *T.* In our low-field MRI device, the time-bandwidth product (TBW) $T\Delta f = 5$, the pulse width *T*=2 ms. Consequently, Δf is 2.5 kHz, Δz is 5 mm, and the maximum gradient amplitude should be larger than 11.74 mT/m. The efficiency is defined as the gradient amplitude generated by the unit current. Our gradient amplifier can provide up to a current of 60 A, thus, the objective of the design is to generate a field with an efficiency greater than 200 μT/(m·A). The non-linearity, defined as:

$$\delta = \left| \frac{\boldsymbol{B} - \boldsymbol{B}_{target}}{\boldsymbol{B}_{target}} \right| \times 100\%, \tag{18}$$

should be less than 5% in a spherical ROI with a diameter of 200 mm. The X-gradient coil was wired on a circular plate with a radius of 300 mm. The distance between the pair of gradient coils was 320 mm. The relative permeability was set at 37200, and the thickness of the equivalent parallel magnetic plates was 10 mm (the same value as the thickness of the anti-eddy plate).

A. Determination of image magnetic dipoles

Computing accuracy improves with an increase in the number of image layers *L* as well as the computation time. Consequently, *L* is determined based on the permeability and thickness of the magnetic plate. As the relative permeability of the magnetic plate is 37200 mm, one image layer would be sufficient to represent the real model because it has a relative error of less than 1%. When the relative permeability of the magnetic plates is lower, *L* must be increased.

B. Determination of regularized coefficient

The regularized coefficient λ is a key parameter that must be carefully determined by considering the design requirements for non-linearity and efficiency. The efficiency, non-linearity, and inductance of the gradient coil as functions of λ are plotted, as seen in Fig. 14. There is a positive correlation between λ and efficiency as well as non-linearity and a negative correlation with the inductance. Moreover, the number of contour lines of stream function N_c, which equals the number of turns in the gradient coil, also influences those quantities; as N_c increases, the efficiency and inductance increase, and in contrast, the non-linearity decreases. Considering the design requirements for the efficiency and linearity, the regularized coefficient λ was chosen to be 10^{-20}, and the number of contour lines N_c was set to 40, with the possible smaller inductance value.

Q is the number of magnetic dipoles (current loops) in the gradient coil area, and *T* is the number of the image magnetic dipoles (image current loops) for a single image layer. *T* always holds the same value as *Q*. Fig.14. (d) shows the dependence of nonlinearity and computation time on *Q*. With the increase of the *Q*, the non-linearity gradually stabilizes and the calculation time gradually increases. This indicates that a *Q* of 40 is sufficient for a design area with a diameter of 600 mm.

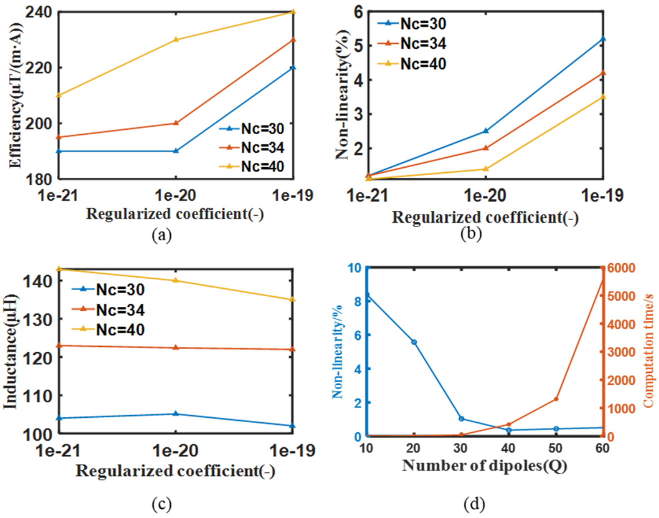

Fig. 14. Dependence of (a) efficiency, (b) mean non-linearity, and (c) inductance on λ, and (d) dependence of nonlinearity and computation time on *Q*.

C. Gradient coil design results

Figs. 15 (a) and (b) show the optimized profile of *S* and its coil pattern, respectively. Fig. 15 (c) shows B_z computed by the image method for the optimal design, which is sufficiently close to the fields shown in Figs. 15 (d) and (e), which are computed using simplified and full models. This indicates that other structures except the anti-eddy plate have negligible effects on the target field. In these three models, their maximum non-linearity of B_z is 3.2%, 3.3% and 3.3%, respectively, and their efficiency have the same value of 240 μT/(m·A). Their performances meet the design requirements [20].

To compare the proposed and conventional design methods, another X gradient coil was designed using the conventional method. The resulting optimal stream function and X gradient coil path are shown in Fig. 16 (a) and (b). It exhibits good linearity when no nearby magnetic materials are present, as shown in Fig. 16 (c). The maximum non-linearity is 4.3%, however, when the gradient coil is placed in the complete model, the magnetic effects distort the gradient field in the target region, as shown in Fig. 16 (d), and the maximum non-linearity is greater than 10%.

The comparation between Fig.15 and Fig.16 illustrates that the proposed method is well capable of taking into account the influence of ferromagnetic materials. Compared with the conventional method, the proposed method provides good linearity even under the effects of surrounding ferromagnetic materials.

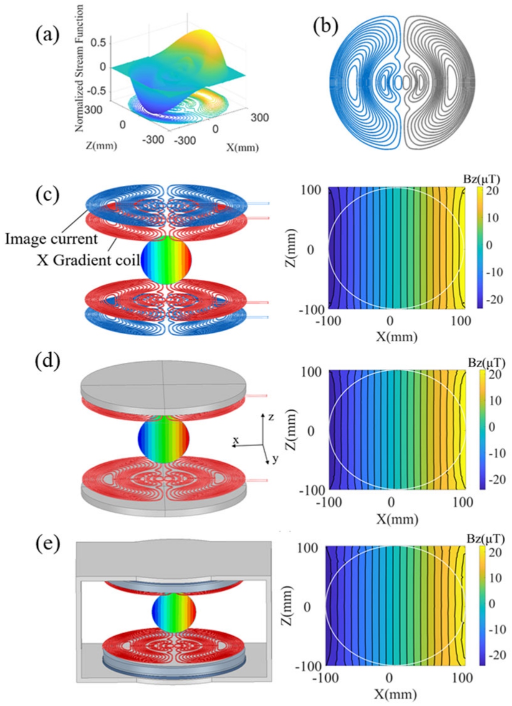

Fig. 15. Design results of the proposed method. (a) and (b) are the optimal stream function and optimal X gradient coil path; (c) (d) and (e) are the simulation results of B_z in the image current model, simplified model (parallel magnetic plates), and full model, respectively.

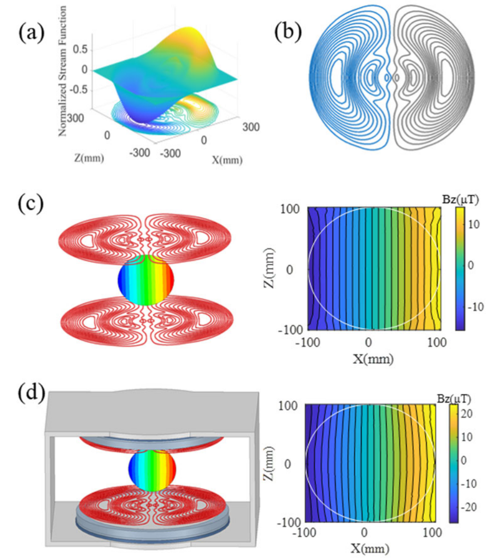

Fig. 16. Design results of the conventional method. (a) and (b) are the optimal stream function and optimal X gradient coil path; (c) and (d) are the simulation results of B_z in the coil-only model and full model, respectively.

V. EXPERIMENTAL VALIDATION

A. *Gradient coils fabrication*

A set of gradient coils were fabricated following the optimization results, as shown in Fig. 17. Regarding the actual winding of the gradient coil, a groove for the coil-winding trajectory was machined on an epoxy resin plate with a thickness of 4 mm and radius of 360 mm. A copper wire was embedded in the groove to form a coil structure for the desired trajectory. The highest current required under normal operating conditions is 60 A. As 1 mm^2 of copper wire can carry a 10 A current and the required cross-section of the wire is 6 mm^2, two copper wires with a cross-section of 2 mm × 1.5 mm were used, which were in parallel winding for easy fabrication.

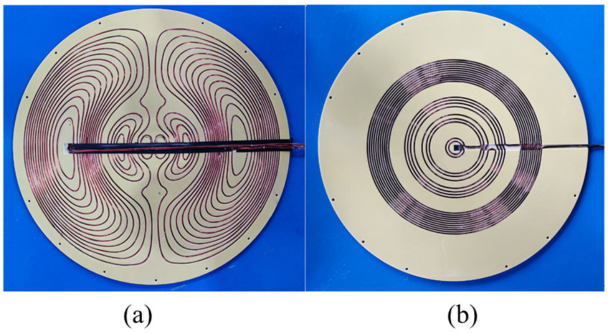
(a) (b)

Fig. 17. Real model of (a) X gradient coil and (b) Z gradient coil (the Y gradient coil has a similar pattern as that of the X gradient coil).

B. *Gradient fields measurements*

The gradient coils were powered by a DC source (6233A, Agilent) with a current of 1 A. B_z in the ROI was measured using the platform depicted in Fig. 18. The field test device was controlled using a Metrolab Precision Nuclear Magnetic Resonance (NMR) Tesla meter (PT2026, resolution: 0.01 ppm in uniform 3 T field, accuracy: ± 5 ppm of field strength). Since there was a strong static magnetic field in the z-direction produced by the magnets, the gradient field was obtained by subtracting the static magnetic field from the total magnetic field.

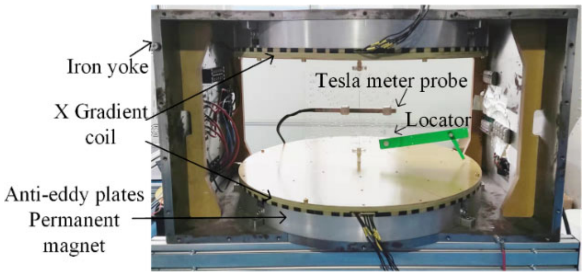

Fig. 18. Magnetic field test platform.

The performance of the proposed method was compared to that of the conventional method. Figs. 19 (a) and (b) show the flux density on the spherical surface of the ROI. Figs. 19(c) and (d) show the distribution of B_z on the central surface of the ROI, where the dotted lines are the reference lines. Here, evident distortions in Figs. 19(b) and 19(d) are noticed, caused by the magnetic effects of the anti-eddy plates. The distortions are corrected using the proposed method, as shown in Figs. 19(a) and (c). Figs. 19(e) and (f) show B_z on the central line of the ROI generated by the coils designed using the proposed and conventional methods. Here, the proposed method has smeller error with ideal gradient field, which means it improves the linearity. In the entire region of the ROI sphere, for the coils obtained using the proposed and conventional methods, the maximum non-linearity of the gradient coil and the efficiency are approximately 4.5%, 242 μT/(m·A) and 10%, 215 μT/(m·A), respectively.

The performance of the Z-gradient coil using measurements was evaluated. Similarly, the Z-gradient field in the ROI produced by the Z-gradient coil designed using the proposed and conventional method was compared. Unlike the X and Y gradient coils, the Z gradient coil had good linearity, even when it is designed using the conventional method. This is because of the symmetrical effects of the anti-eddy plates on the Z gradient field.

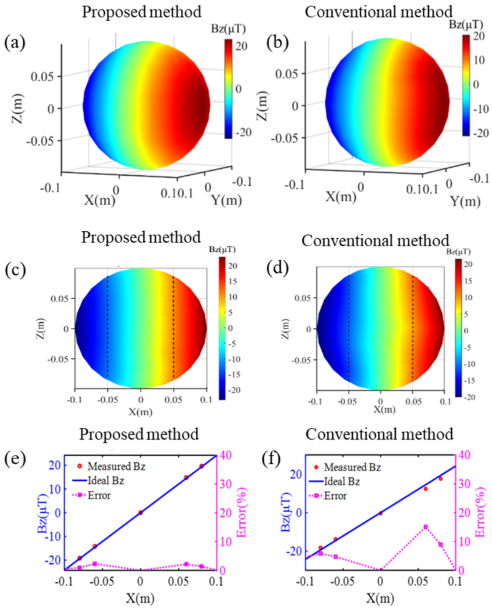

Fig. 19. Comparison of the performances X gradients designed by the proposed method and conventional method. (a) and (b) show the distribution of B_z on the spherical surface of ROI; (c) and (d) show the distribution of B_z on the central surface of the ROI; (e) and (f) show B_z along the central line of ROI.

Figs. 20(a) and (b) show the flux density on the spherical surface of the ROI for the proposed and conventional methods, respectively. Figs. 20(c) and (d) show the distribution of B_z on the central surface of the ROI for the proposed and conventional methods, respectively, where the dotted lines represent the reference lines. Fig. 20(e) portrays B_z on the central line of the ROI generated by the coils designed using the proposed and conventional methods. From the above figures, both the proposed and conventional coils have good linearity. In the entire region of the ROI sphere, for the Z gradient coil designed using the proposed and conventional methods, the maximum non-linearity and efficiency are approximately 3.2%, 274 μT/(m·A) and 4.7%, 244 μT/(m·A), respectively. The proposed and conventional methods do not reveal any considerable magnetic field distortion. Owing to the rotationally symmetrical effects of the anti-eddy plates on the Z gradient field, the Z gradient field is less vulnerable to the influence of ferromagnetic materials than the X and Y gradient fields.

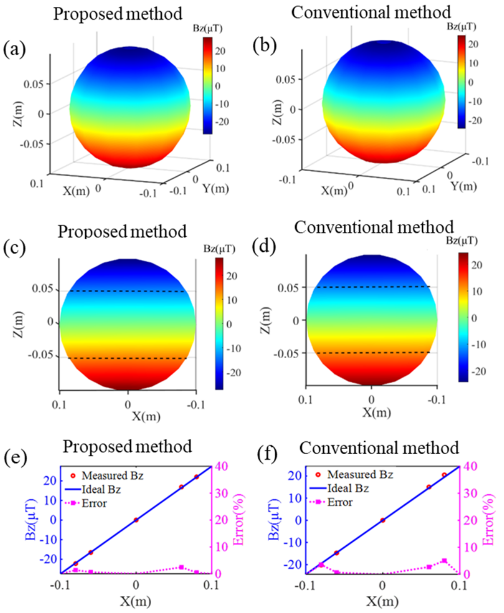

Fig. 20. Comparison of the performances Z gradients deigned by the proposed method and conventional method. (a) and (b) show the distribution of B_z on the spherical surface of ROI; (c) and (d) show the distribution of B_z on the central surface of the ROI; (e) and (f) show B_z along the central line of ROI.

Table III lists the detailed parameters of the gradient coils designed using the proposed method when the coils were installed in the devices.

TABLE III
MEASURED PARAMETERS OF GRADIENT COILS BY THE PROPOSED METHOD

	X	*Y*	*Z*
Resistance (mΩ)	101.0	101.2	56.6
Inductance (μH)	141.3	141.5	87.5
Efficiency (μT/(m·A))	242	242	274
Average non-linearity (%)	2.3	2.2	1.6
Maximum non-linearity (%)	4.5	4.2	3.2

The experimental results reveal that the X- and Z-gradient coils designed using the proposed method produce gradient field with good linearity, even under the influence of nearby magnetic materials. Negligible distinctions are observed between the measurements and calculations owing to fabrication and measurement errors. Thus, the measurement results meet the design requirements. This indicates the validity and feasibility of the proposed method.

C. Imaging results comparison

The coils designed using the conventional and proposed methods were installed on similar low-field NMR equipment, and phantom imaging experiments were performed.

The 50 mT low-field MRI device was placed on the shielding open area and the active denoising method [4] was utilized to reduce the environmental noise, as shown in Fig. 21. Phantom (CuSO4·5H2O, 1.95 g/L) and human brain images are shown in Fig. 22. With the gradient coils designed using the proposed method, image distortion was considerably reduced in the target area compared to that of the conventional method.

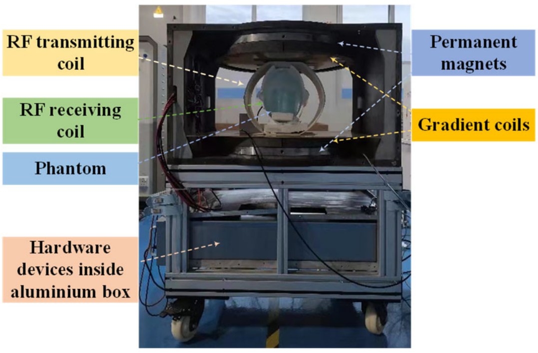

Fig. 21. Unshielded 50 mT low-field MRI device.

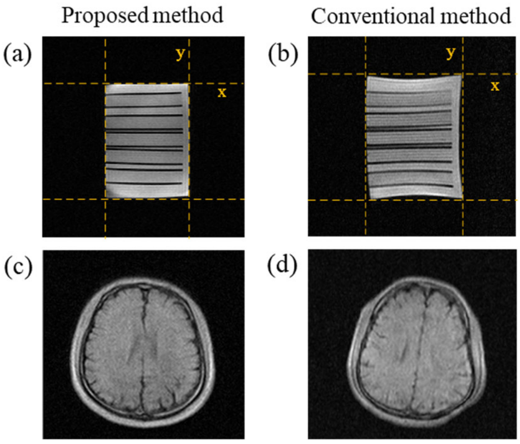

Fig. 22. Imaging results comparison between the proposed method and the conventional method. (a) and (b) show the T1-weighted images in the x-y plane of the phantom (CuSO4·5H2O, 1.95 g/L) with small cylindrical tubes. The yellow dotted lines are used as the reference lines. (c) and (d) show the T1-weighted images in the x-z plane (transverse) of the human brain. 3D Gradient Recalled Echo (GRE) sequence was utilized for T1-weighted imaging. These images were acquired in 1 min 3 s, with a slice thickness of 10 mm. Number slices = 4, echo time [TE] = 21 ms, repetition time [TR] = 46 ms, number of averages = 1, resolution = 1.5 × 1.5 × 10 mm^3, and field of view: 250 mm × 250 mm.

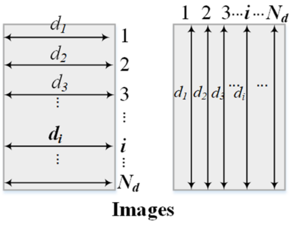

Fig. 23. Schematic picture of the image distortion evaluation method.

To quantify the imaging distortion, the geometric distortion δ and aberration geometric distortion σ_δ [30] were evaluated as follows:

$$\delta = \left(1 - \frac{\bar{d}}{D}\right) * 100\%, \tag{19}$$

$$\sigma_\delta = \frac{1}{D}\sqrt{\frac{\sum_{i=1}^{Nd}\left(d_i - \bar{d}\right)^2}{N_d - 1}} * 100\%, \tag{20}$$

where N_d represents the number of measured lines, D is the real length of the test phantom, d_i is the measured length, and $\bar{d}$ is the mean value of the measured length, as shown in Fig. 23. Table IV summarizes the geometric distortion and aberration geometric distortion in the x- and y-directions.

TABLE IV
DISTORTION EVALUATION

	δ (%) (x-direction)	δ (%) (y-direction)	σ_δ (%) (x-direction)	σ_δ (%) (y-direction)
Proposed method	1.1	0.8	1.2	0.9
Conventional method	4.3	4.7	5.0	5.8

For the conventional method, the geometric distortion δ in the x- and y-directions is more than 4% and the aberration geometric distortion is more than 5%. For the proposed method, the geometric distortion δ and aberration geometric distortion are both less than 1.2%, suggesting that the image distortion is effectively mitigated by the proposed design method.

VI. CONCLUSION

A novel method for designing gradient coils for low-field MRI devices was proposed. The proposed method considered the effect of magnetic materials, particularly anti-eddy plates, by introducing image dipole currents. In the optimal design of gradient coils, the effect of ferromagnetic materials was minimized to obtain highly linear fields. The magnetic field measurement results and phantom images revealed the validity of the proposed method.

APPENDIX

This appendix describes the analytical method used for the homogenized model of laminated structures. The solenoid model is portrayed in Fig. 24 and 25.

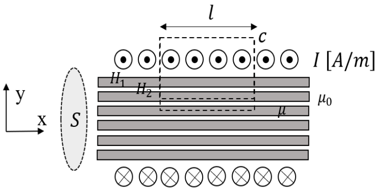

Fig. 24. Solenoid model (Model A) used to calculate the homogenized permeability in the laminated direction.

As shown in Fig. 24, the laminated structure (gray) has a permeability of μ, which is inside the infinite-long solenoid, with each wire carrying a similar current *I*. On the solenoid, the magnetic field is nearly homogeneous and parallel to the *x*-direction, whereas the field is negligibly small outside the solenoid. The magnetic fields in the steel sheet and air gap are denoted as H_1 and H_2. The filling rate (volume fraction) of the laminated structure is expressed as α and calculated as:

$$\alpha = \frac{t_{steel}}{t_{steel} + t_{gap}} \tag{A1}$$

Model A is used to calculate the homogenized permeability along the laminated direction (*x*-direction) $\mu_\parallel$. Applying Ampere's Law to a closed-loop *c* with length *l*, we obtained:

$$\oint_c \boldsymbol{H} \cdot d\boldsymbol{s} = lI \tag{A2}$$

We had:

$$lH_1 = lI,\ lH_2 = lI. \tag{A3}$$

Evidently:

$$H_1 = I,\ H_2 = I. \tag{A4}$$

The total magnetic flux along the *x*-direction inside the coil:

$$\begin{aligned} \Phi = SB &= S\{\alpha\mu H_1 + (1-\alpha)\mu_0 H_2\} \qquad \text{(A5)} \\ &= SI\{\alpha\mu + (1-\alpha)\mu_0\}, \end{aligned}$$

where *S* is the cross-sectional area of the solenoid. Assuming homogenized parallel permeability $\mu_\parallel$, the total flux is as follows:

$$\Phi = SB = \mu_\parallel SI \tag{A6}$$

From (A6) and (A7), the homogenized permeability along the lamination direction $\mu_\parallel$ is represented as follows:

$$\mu_\parallel = \alpha\mu + (1-\alpha)\mu_0 \tag{A7}$$

The homogenized relative permeability along the laminated direction is defined as $\mu_{\parallel r}$, which can be obtained from:

$$\mu_{\parallel r} = \frac{\mu_\parallel}{\mu_0}. \tag{A8}$$

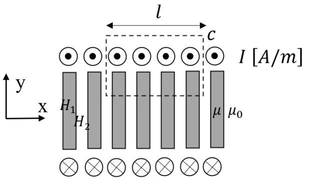

Fig. 25. Solenoid model (Model B) used to calculate the homogenized permeability in the perpendicular direction.

Model B, as depicted in Fig. 25, is used to calculate the homogenized permeability in the perpendicular direction $\mu_\perp$. The following is derived from Ampere's law:

$$\alpha H_1 + (1-\alpha)H_2 = I. \tag{A9}$$

Equation (A10) is obtained as the magnetic flux density *B* inside the solenoid coil along the x-direction is constant:

$$B = \mu H_1 = \mu_0 H_2. \tag{A10}$$

Combining (A9) and (A10), the following is obtained:

$$\left(\frac{\alpha}{\mu} + \frac{1-\alpha}{\mu_0}\right) B = I. \tag{A11}$$

The magnetic flux density *B* is represented as:

$$B = \frac{\mu\mu_0 I}{\alpha\mu_0 + (1-\alpha)\mu}. \tag{A12}$$

When the homogenized material with permeability $\mu_\perp$ is considered, the magnetic flux density is:

$$B = \mu_\perp I \tag{A13}$$

From (A12) and (A13), the homogenized permeability in the perpendicular direction $\mu_\perp$is expressed as:

$$\mu_\perp = \frac{\mu\mu_0}{\alpha\mu_0 + (1-\alpha)\mu}. \tag{A14}$$

Similarly, the relative permeability along the perpendicular direction is defined as $\mu_{\perp r}$, which is obtained from:

$$\mu_{\perp r} = \frac{\mu_\perp}{\mu_0} \tag{A15}$$

REFERENCES

[1] Y. Liu, Y. Shi, F. Mu, J. Cheng, C. Li and X. Chen. "Multimodal MRI Volumetric Data Fusion With Convolutional Neural Networks," IEEE *Trans. Instrum. Meas.*, vol. 71, pp. 1-15, Jun.2022, doi: 10.1109/TIM.2022.3184360.

[2] G. Andria, F. Attivissimo, G. Cavone and A. M. L. Lanzolla, "Acquisition Times in Magnetic Resonance Imaging: Optimization in Clinical Use," IEEE *Trans. Instrum. Meas.*, vol. 58, no. 9, pp. 3140-3148, Sep. 2009, doi: 10.1109/TIM.2009.2016888.

[3] M. H. Mazurek, B. A. Cahn, M. M. Yuen, et al. "Portable, bedside, low-field magnetic resonance imaging for evaluation of intracerebral hemorrhage," *Nat. Commun.*, vol. 12, no. 1, pp. 5119, Aug.2021, doi: https://doi.org/10.1038/s41467-021-25441-6.

[4] L. Yang, W. He, Y. He, J. Wu, S. Shen, and Z. Xu. "Active EMI Suppression System for a 50 mT Unshielded Portable MRI Scanner," *IEEE Transactions on Biomedical Engineering.*, vol. 1, no. 1, Apr. 2022, doi: 10.1109/TBME.2022.3170450.

[5] Liu, Y., Leong, A.T.L., Zhao, Y. et al. "A low-cost and shielding-free ultra-low-field brain MRI scanner," *Nat Commun.*, vol. 12, no. 1, pp. 7238, Dec. 2021, doi: https://doi.org/10.1038/s41467-021-27317-1.

[6] Huang, X. et al. "Adaptive suppression of power line interference in ultra-low field magnetic resonance imaging in an unshielded environment," *J. Magn. Reson.,* vol. 286, pp. 52-59, Jan. 2018, doi: https://doi.org/10.1016/j.jmr.2017.11.009.

[7] Campbell-Washburn, A. E., Ramasawmy, R., Restivo, M. C. et al. "Opportunities in interventional and diagnostic imaging by using high-performance low-field-strength MRI," *RADIOLOGY*, vol. 293, no. 2, pp. 384-393, Oct. 2019, doi: https://doi.org/10.1148/radiol.2019190452.

[8] Sarracenia, M. et al. "Low-cost high-performance MRI," *Sci. Rep*., vol. 15, no. 5, pp. 15177, Oct. 2015, doi: https://doi.org/10.1038/srep15177.

[9] Lother S, Schiff SJ, Neuberger T, Jakob PM, Fidler F. "Design of a mobile, homogeneous, and efficient electromagnet with a large field of view for neonatal low-field MRI," *MAGMA*. vol. 29, no. 4, pp. 691-8, Aug. 2016, doi: 10.1007/s10334-016-0525-8

[10] Choquet P, Breton E, Goetz C, Marin C, Constantinesco A. "Dedicated low-field MRI in mice," *Phys Med Biol*., vol.54, no. 17, pp. 5287-99, Aug.2009, doi: 10.1088/0031-9155/54/17/014.

[11] Cooley, C. Z. et al. "A portable scanner for magnetic resonance imaging of the brain," *Nat. Biomed. Eng*., vol. 5, no. 3, pp. 229–239, Mar. 2021, doi: 10.1038/s41551-020-00641-5.

[12] O'Reilly, T., Teeuwisse, W. M., de Gans, D., Koolstra, K. & Webb, A. G. "In vivo 3D brain and extremity MRI at 50 mT using a permanent magnet Halbach array," *Magn. Reson. Med*., vol. 8, no. 1, pp. 495–505, Jan. 2021, doi: https://doi.org/10.1002/mrm.28396.

[13] Danieli E, Mauler J, Perlo J, Blümich B, Casanova F. "Mobile sensor for high resolution NMR spectroscopy and imaging," *J Magn Reson*., vol.198, no. 1, pp.80-7, Jan. 2009, doi: https://doi.org/10.1016/j.jmr.2009.01.022.

[14] He, Y. et al. "Use of 2.1 MHz MRI scanner for brain imaging and its preliminary results in stroke," *J. Magn. Reson.,* vol. 319, pp.106829, Oct. 2020, doi: 10.1016/j.jmr.2020.106829.

[15] Wright, S.M., Brown, D.G., Porter, J.R. et al. "A desktop magnetic resonance imaging system," *MAGMA,* vol. 13, no. 3, pp.177–185, Aug. 2001, doi: https://doi.org/10.1007/BF02678594.

[16] Yoshioka, Hiroshi, Ito, Satoshi, Handa, et al. "Low-field compact magnetic resonance imaging system for the hand and wrist in rheumatoid arthritis," *Journal of magnetic resonance imaging*, vol. 3, no. 23, pp. 370-376, Feb. 2006, doi: https://doi.org/10.1002/jmri.20501.

[17] McDaniel PC, Cooley CZ, Stockmann JP, Wald LL. "The MR Cap: A single-sided MRI system designed for potential point-of-care limited field-of-view brain imaging," *Magnetic Resonance in Medicine*, vol. 82, no. 5, pp. 1946-1960, Nov. 2019, doi: https://doi.org/10.1002/mrm.27861.

[18] F. Zhao, X. Zhou, X. Xie and K. Wang, "Design of Gradient Magnetic Field Coil Based on an Improved Particle Swarm Optimization Algorithm for Magnetocardiography Systems, " IEEE *Trans. Instrum. Meas.*, vol. 70, pp. 1-9, Aug. 2021, doi: 10.1109/TIM.2021.3106677.

[19] Dardo Tomasi. "Stream function optimization for gradient coil design," *Magnetic Resonance in Medicine*, vol. 45, no. 3, pp. 505 – 512, Mar. 2001, doi: https://doi.org/10.1002/1522-2594(200103)45:3<505::AID-MRM1066>3.0.CO;2-H.

[20] Turner. "A target field approach to optimal coil design," *J. Phys. D.,* vol. 19, pp. L147-L151, May. 1986, doi: 10.1088/0022-3727/19/8/001.

[21] Z. Ding, Z. Huang, M. Pang and B. Han, "Design of Bi-Planar Coil for Acquiring Near-Zero Magnetic Environment," IEEE *Trans. Instrum. Meas*, vol. 71, pp. 1-10, Feb. 2022, doi: 10.1109/TIM.2022.3151939.

[22] H. S. Lopez. "Equivalent Magnetization Current Method Applied to the Design of Gradient Coils for Magnetic Resonance Imaging," *IEEE Trans. Magn.,* vol.45, no. 2, pp. 767-775, Feb. 2009, doi: 10.1109/TMAG.2008.2010053.

[23] M. A. Brideson, L. K. Forbes, and Crozier S. "Determining complicated winding patterns for shim coils using stream functions and the target-field method," *Concepts in Magnetic Resonance Part A*, vol. 14, no. 1, pp. 9-18, Jan. 2002, doi: 10.1002/cmr.10000.

[24] Xu, Zheng and Qi, Jinfeng. "Equivalent magnetic dipole method for designing gradient coils of the Halbach magnetic resonance device". *International Journal of Applied Electromagnetics and Mechanics*. Vol.56. pp.595-604, Jan. 2018, doi: 10.3233/JAE-170115.

[25] J. Yang, X. Zhang, B. Han, J. Wang and L. Wang, "Design of Biplanar Coils for Degrading Residual Field in Magnetic Shielding Room, " IEEE *Trans. Instrum. Meas.*, vol. 70, pp. 1-10, 2021, doi: 10.1109/TIM.2021.3108493.

[26] F. Zhao, X. Zhou, W. Zhou, X. Zhang, K. Wang and W. Wang, "Research on the Design of Axial Uniform Coils for Residual Field Compensation in Magnetically Shielded Cylinder, " IEEE *Trans. Instrum. Meas.*, vol. 71, pp. 1-9, 2022, doi: 10.1109/TIM.2022.3188525.

[27] W. A. Roshena and D. E. Turcotte. "Planar inductors on magnetic substrates," *IEEE Trans. Magn.,* vol.24, no. 6, pp. 3213-3216, doi: 10.1109/20.92379.

[28] W. A. Roshen. "Effect of finite thickness of magnetic substrate on planar inductors," *IEEE Trans. Magn.,* vol. 26, no. 1, pp. 270-275, Jan. 1990, doi: 10.1109/20.50553.

[29] M. A. Bernstein, K. F. King, X. J. Zhou., "Handbook of MRI pulse sequences.", Elsevier Academic Press, MA, USA,2004, pp:104-105.

[30] Magnetic resonance equipment for medical imaging - Part 1: Determination of essential image quality parameters, IEC 62464-1, 2007.

Xiaohan Kong was born in Shandong, China, in 1994. She received the B.Sc. and M.Sc. degrees from Chongqing University, Chongqing, China, in 2016 and 2020, respectively. She is currently pursuing the Ph.D. degree at Hokkaido University, Sapporo, Japan. Her research interests include computational electromagnetism, design optimization of electromagnetic structures, and magnetic resonance imaging (MRI).

Zheng Xu was born in Jiangsu, China, in 1980. He received the B.Sc., M.Sc., and Ph.D. degrees from Chongqing University, Chongqing, China, in 2002, 2005, and 2008, respectively, all in electrical engineering. He is currently a Professor with the School of Electrical Engineering, Chongqing University. His research areas include designing the magnet structure and RF coil for the NMR/MRI system.

Sheng Shen was born in Anhui, China, in 1993. He received the B.Sc degree from Liaoning University, (Liaoning, China) in 2016, and received the Ph.D. degree from Chongqing University (Chongqing, China) in 2021. He is currently a postdoctoral research follow in MGH/Martinos center and Harvard Medical School, USA. His research areas include electromagnetic calculation, sensor technologies, magnetic resonance physics, ultra-low field MRI.

Jiamin Wu received D.E. degree in electric engineering from Chongqing University in 2019. Currently engaged in post-doctoral research in Shenzhen Aerospace Science and Technology Innovation Institute. His research interest includes Electromagnetic field calculation, magnetic resonance imaging (MRI) and magnet designing for MRI.

Yucheng He received the D.E. degree in electric engineering from Chongqing University in 2020. Currently engaged in post-doctoral research in Shenzhen Aerospace Science and Technology Innovation Institute. His research interest includes magnetic resonance imaging (MRI) methods and RF coil designing.

Liang Xuan received the bachelor's degree and the master's degree in electrical engineering from Wuhan University, Wuhan, China, in 2016 and 2018 respectively, where he is currently pursuing the doctor's degree in Chongqing University, Chongqing, China. His major research area includes computational electromagnetics, magnetic components design for magnetic resonance imaging.

Hajime Igarashi (Member, IEEE) received the B.E. and M.E. degrees in electrical engineering and the Ph.D. degree in engineering from Hokkaido University, Sapporo, Japan, in 1982,1984, and 1992, respectively. He has been a Professor with the Graduate School of Information Science and Technology, Hokkaido University, since 2004. His research interests include computational electromagnetism, design optimization, and Artificial Intelligence (AI)-based design. Dr. Igarashi is a vice president of the International Compumag Society, a member of the Institute of Electrical Engineers of Japan (IEEJ), the Institute of Electronics, the Information and Communication Engineers (IEICE) and Japan Society of Applied Electromagnetics and Mechanics (AEM).